LCLS-II Technical Note

Cornell LCLC-II Collaboration Report

LCLSII-TN-15-21

6/25/2015

C. Gulliford, A. Bartnik, I. Bazarov, L. Cultrera, B. Dunham, J. Maxson
Cornell University, 161 Synchrotron, Ithaca, NY, 14853, USA

SLAC NATIONAL ACCELERATOR LABORATORY
BERKELEY LAB
Argonne NATIONAL LABORATORY
CORNELL UNIVERSITY FOUNDED A.D. 1865
Fermilab
Jefferson Lab

Cornell LCLS-II Collaboration Report

Colwyn Gulliford, Adam Bartnik, Ivan Bazarov, Luca Cultrera, Bruce Dunham, and Jared Maxson
CLASSE, Cornell University, 161 Synchrotron Drive Ithaca, NY 14853-8001
(Dated: June 25, 2015)

I. CORNELL INJECTOR MEASUREMENTS

The main priority of the experimental portion of the injector collaboration was to demonstrate that the Cornell injector can meet the beam requirements for the proposed LCLS-II Injector shown in Table-1. Fig. 1 shows the current layout of the Cornell injector, a 5-15 MeV photoelectron source originally designed to create low emittance, moderate bunch charge ($\leq$77 pC) beams at high (1.3 GHz) repetition rate for a full hard x-ray ERL. Currently, the Cornell injector holds the world record for high average current from a photoinjector with cathode lifetimes suitable for an operating user facility [1], as well as the record for lowest demonstrated emittance from a DC gun-based photoinjector at bunch charges of 19 and 77 pC [2]. The current injector layout is largely unchanged from previous experiments [1, 2], with the exception of the removal of the merger section used in previous low emittance measurements [2]. While the previous emittance measurements in [2] roughly satisfy the 95% emittance specifications for the 20 and 100 pC bunch charge specifications, it remained to be seen if both the peak current and emittance specifications could be met simultaneously for all three target charges.

TABLE I. LCLS-II Injector Specifications

Bunch Charge	20 pC	100 pC	300 pC
95% $\epsilon_{n,x,y}$	0.25 μm	0.40 μm	0.60 μm
Peak Current	5 A	10 A	30 A

For this work, we measured all of the direct phase space and longitudinal profile data using a two slit interceptive Emittance Measurement System [2, 3] (EMS). To limit the beam powered deposited into the first EMS slit, we exclusively used a 50 MHz laser. This system produces 520 nm, 1 ps rms pulses with comparable pulse energy to the primary 1.3 GHz laser used for full repetition rate experiments [4]. Four rotatable birefringent crystals (lengths: 15.096, 7.5480, 3.7740, 1.8870 mm) temporally shape the primary pulses by splitting each into 16 copies with tunable relative intensities set by the crystal rotation angles. For transverse shaping, we used a beam expander and pinhole to clip the Gaussian laser distribution at roughly the half maximum intensity (truncation fraction of 50%). As part of preparations for emittance measurements, the single insulator DC gun used in the injector was HV processed up to 440 kV in order to run reliably around 400 kV. This was checked by operating the gun at 395 kV for 48 hours, during which time no HV trips were experienced. For all measurements reported here, we used a single NaKSb cathode [5] with a 140 ± 10 meV cathode mean transverse energy (MTE), as measured using a solenoid scan procedure [6]. MTE data taken with the gun operating at 250 kV, 300 kV, and 350 kV showed no measurable dependence of the MTE with gun voltage.

A. Experimental Set-up

In order to determine the injector settings that produce optimal emittances and peak currents, we ran Multi-Objective Genetic Algorithm (MOGA) optimizations using the 3D space charge code General Particle Tracer (GPT) [7]. For each of the LCLS-II nominal charges, the optimizer simultaneously minimized both the emittance and rms bunch length at the location of the EMS in the simulated injector, subject to realistic constraints on all relevant injector and beam parameters. For a detailed description of our 3D injector model, refer to [2]. Additionally, we provided the optimizer with a realistic simulation of the laser distribution, and allowed the optimizer to vary the transverse pinhole size and truncation fraction, as well as the rotation of the longitudinal shaping crystal angles.

The resulting Pareto fronts (shown later) provided injector settings that simultaneously satisfied both the 95% emittance and peak current goals specified by the LCLS-II injector design. In all cases, the optimizer chose a 9-9.5 MeV final beam energy at the EMS. Additionally, the optimizer chose 0.73 mm, 1.9 mm, and 3.5 mm pinhole diameters, and roughly 50% for the truncation fraction for the three bunch charges respectively. The corresponding pinholes available at the time of measurement were 1 mm, 2 mm, and 3.5 mm. Post processing of the optimized simulations showed a weak dependence of the transverse emittances on the temporal shaping crystal angles. For simplicity, we tuned the crystal angles to produce a flat top temporally.

1. Laser Characterization

In order to characterize the initial temporal laser shape, we measured the longitudinal electron beam current profile at near zero charge (0.02 $\pm$ 0.01 pC) with all RF cavities off. Finally, we loaded the corresponding machine settings and measured laser distributions for each bunch charge into our virtual accelerator GUI [2], and ran 250k macro-particle GPT simulations for com-

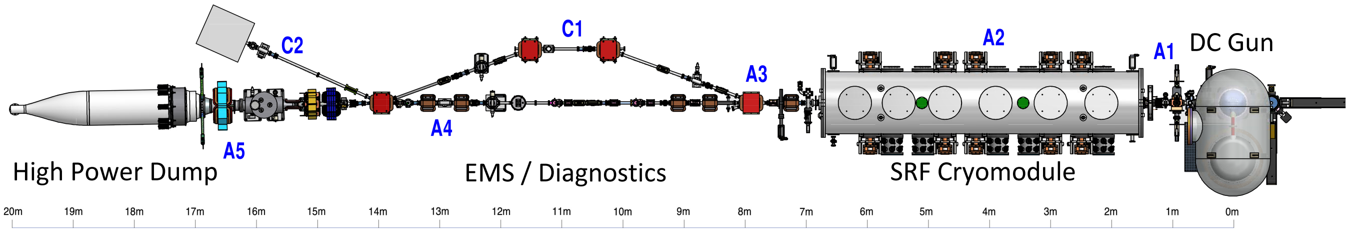

FIG. 1. Top view of the Cornell ERL injector.

TABLE II. Injector Settings

Parameter	20 pC	100 pC	300 pC
Laser Pinhole, RMS bunch length (mm, ps)	1, 8	2, 8	3.5, 8
Solenoid 1Current (A)	-4.13	-4.04	-3.98
Buncher Voltage, Phase (kV, deg)	63, -90	64, -90	85, -90
Solenoid 2 Current (A)	2.18	2.33	2.58
SRF Cavity 1 Voltage, Phase (kV, deg)	2100, -10	2100, -10	2100, -10
SRF Cavity 2 Voltage, Phase (kV, deg)	1000, -20	1000, -20	1000, -20
SRF Cavity 3 Voltage, Phase (kV, deg)	2300, -10	2300, -10	2300, -10
SRF Cavity 4 Voltage, Phase (kV, deg)	1700, -10	1700, -10	1700, -10
SRF Cavity 5 Voltage, Phase (kV, deg)	2000, -30	2000, -30	2000, -30
A3 Quad 1 Current (A)	-1.5	-1.5	-1.5
A4 Quad 2 Curent (A)	1.5	1.5	1.5

parison with measurement. Fig. 2 shows the measured laser distributions on a CCD camera located at the same distance from the clipping pinhole as the cathode. To

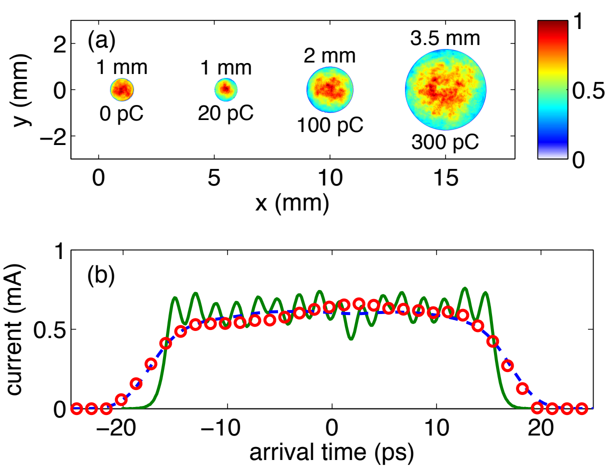

FIG. 2. (a) The measured transverse laser distributions. (b) The simulated temporal laser distribution (green), the resulting electron current profile at the EMS from GPT (dashed blue), and the measured electron current profile (red).

match the optimization results as best as possible, we tuned the laser spot size on the laser CCD so that the edge truncation fraction was 50% using a beam expander. Fig. 2(b) shows the measured temporal current profile of the electron beam at the EMS (red), for a bunch charge of 0.02 ± 0.01 pC, and with all RF cavities off. The green curve shows the simulated initial temporal laser distribution (normalized to 0.02 pC) and the resulting simulated electron beam current profile at the location of the EMS in GPT (dashed blue).

2. *EMS Thermal Emittance*

The largest source of error in the EMS measurements is the calibration of the scanner magnets. Using a downstream viewscreen, the EMS scanner magnets were calibrated at the target energy of 9 MeV. To verify this calibration, the emittance of the beam at near zero charge was measured using the EMS and compared to the value at the cathode, computed using Eq. 1 and the laser distribution measured by diverting the laser beam to a CCD. Both values agreed within a few percent.

$$\epsilon_{\mathrm{cathode}} = \sigma_{\mathrm{laser}} \sqrt{\frac{\mathrm{MTE}}{m_e c^2}} \tag{1}$$

Once calibrated, the EMS measurement of the thermal emittance is a valuable tool to verify the alignment of the various optics in the beamline. Without the effect of space charge, the emittance of the beam is conserved

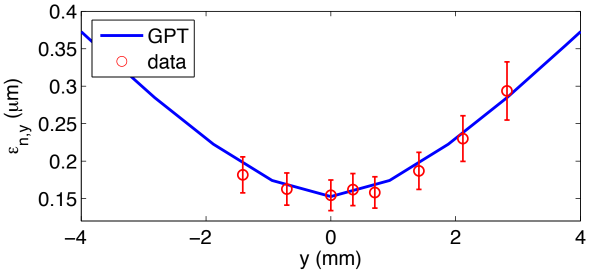

FIG. 3. Measured and simulated vertical emittance as a function of misalignment going into the first SRF cavity, set oncrest at 1500 kV cavity voltage. All other SRF cavities were off.

along the beamline, unless one has aberrations from misaligned optics. As both another check of the EMS system itself, and also to verify the cavity field maps used in GPT, we intentionally misaligned the beam through the first SRF cavity using the last steering magnet before it, keeping all others cavities turned off. In simulation, we modeled the same situation, including a model of the steering magnet. As seen in Fig. 3, the thermal emittance grows just as expected from simulation.

3. Stray Quadrupole Fields in the Solenoid

Initial measurements at 20 pC produced asymmetric horizontal and vertical emittance values, similar to those reported in previous emittance measurements in the merger section. Previously, this asymmetry was suspected to be due to the horizontal bends that the beam takes in the merger, however this could no longer explain the asymmetry seen in the straight section. We initially thought the asymmetry was due to misalignment in the gun, solenoids, buncher, or first two srf cavities. Subsequent attempts at realigning the beam through these elements did not reduced the asymmetry. Further investigation lead to the discovery of an asymmetric beam spot on the first view screen (for bunch charges with at least 10 pC) when the solenoid was tuned to put the beam near a focus on the first viewscreen. Below that charge, due to the optics layout, the beam could not be strongly focused, and the asymmetry was not noticeable to the eye.

Varying the solenoid current changed not only the size of the elliptical beam spot on the viewscreen, but also the orientation of the ellipse. We also noticed that the semi-major axes of the elliptical beam profile aligned perfectly with the kick axes of the horizontal and vertical corrector magnets at the solenoid center, suggesting the ellipse orientation was exactly half of the Larmor angle, as shown in Fig. 4(a). This suggested the presence of a stray quadrupole moment at the solenoid center [8].

Modeling this effect in GPT allowed for the estimation of the stray quad strength by fitting to the measured transverse second moments of the beam on the first viewscreen as a function of the solenoid current. Fig. 4(b) displays the results of the fits. Assuming a 3 inch effective quad length resulted in a roughly 0.5 G/m quadrupole gradient at a solenoid current around 3 A. By doing this fitting procedure at different gun voltages (allowing the beam to focus at different solenoid currents), and also by checking the other polarity of the solenoid magnet, we were able to verify that the strength of the quad field scales linearly with the applied solenoid current.

A temporary correction to this problem was found by using the available holes in the solenoid magnet frame, originally intended as BPM wire feedthroughs, to wire a single-turn correction quad. The field from this type of magnet may be roughly estimated using:

$$B_x = \frac{2(NI)\mu_0}{\pi R^2} y \tag{2}$$

$$B_y = \frac{2(NI)\mu_0}{\pi R^2} x \tag{3}$$

From these expressions, it was estimated that roughly 40 Amp-turns of coil are required to cancel the field given the coil radius of 6 inches, and a length of 3 inches. Correcting coils were wired through both solenoids in the injector, as seen in Fig. 5.

We set the correcting quad coil power supply to scale automatically with the solenoid power supply, with an adjustable scale factor determined by making the beam as round as possible on the viewscreen. Fig. 4(a) shows the resulting beam spots after correction. The corrector coils successfully removed the solenoid dependent tilt of the beam spot, effectively a skew quad, however we still note some remaining x-y asymmetry in the beam spot, perhaps due to a (normal) quadrupole field from the downstream ion pump. We did not attempt to correct this additional remaining stray field, hoping that the effect of this non-skew quad might be cancelled by adjusting the downstream quads in the measurement section.

The same fitting procedure was not done for the second solenoid because the nearest viewscreen is located after the SRF cavities, over 6 m downstream, a distance too far to allow for a reliable measurement at 395 kV beam energy. For this magnet we used roughly the same scale factor with solenoid current to determine its correcting coil current, but allow this parameter to be adjusted while searching for minimum emittances.

4. Faraday Cup Selection

The injector has two Faraday cups that can be used to collect the charge during emittance measurements: one in the middle of the A4 section after the second EMS slit and one after the 20^o bend in the C2 section. Ideally, if all of the charge is correctly guided to either Faraday cup, the measured phase space should be independent of which Faraday cup is used, as the same EMS slits in the A4 sections are used to clip the beam in both cases. In practice however, we found a systematic discrepancy

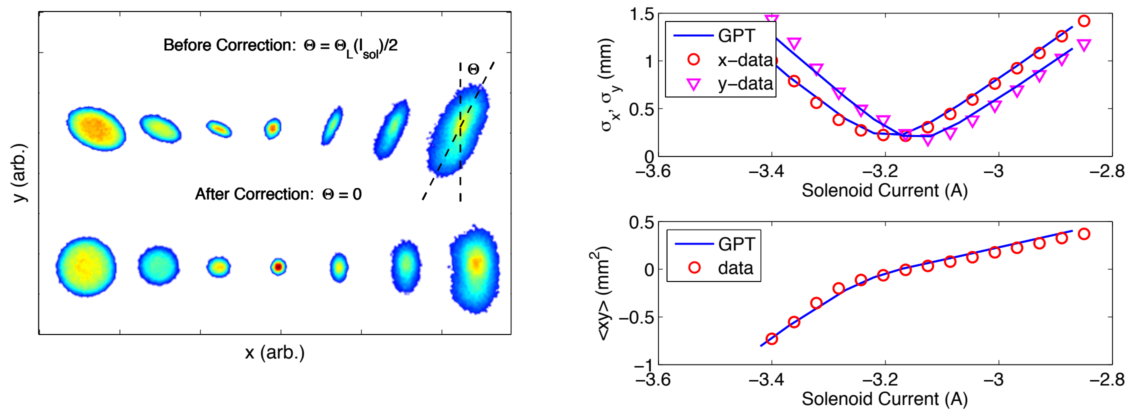

(a) Beam spot on the first viewscreen.

(b) RMS spot sizes σ_x and σ_y, and correlation $\langle xy \rangle$ on the first viewscreen.

FIG. 4. Characterization and correction of the quadrupole moment in the first solenoid. (a) Elliptical beam spot on the first viewscreen after the first solenoid. The tilt of the ellipse was exactly half the Larmor angle of the solenoid. (b) Fitting the measured second moments of the beam spot on the first viewscreen to GPT to estimate the quad strength.

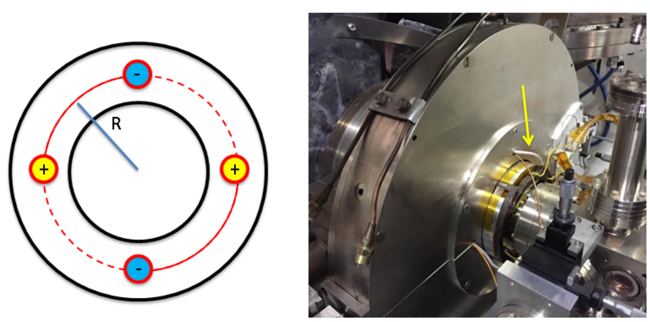

FIG. 5. Wiring of the correction quadrupole magnet, and photo of the wiring as installed. The single turn of wire is indicated with an arrow.

between subsequent measurements using both Faraday cups.

Fig. 6 shows an example phase space measured using both the A4 and C2 Faraday cups. The majority of the phase space is identical in both cases, but when using the A4 Faraday cup, there is always a vertical smearing, producing a shadow-like background mostly below the core of the phase space. We were unable to determine the cause of this, but believe this to be an artifact of the measurement. We tried changing which axis of the phase space is scanned quickly, to see if the smearing is somehow due to the rapid changing of the scanner magnets, but the shadow was always in the same place. We verified that there was no beam lost as when sending the beam into the C2 Faraday cup by moving all corrector dipoles over large ranges, and seeing no change in the measured phase space. We speculate that the spurious background is due to secondary electrons produced in the Faraday cup from radiation that penetrates the second EMS slit. This slit does not have the same armor beamstop material around the slit opening like the 1st slit [3], and would be more likely to have radiation leaking through it. Bending the remaining electrons into the C2 section, separates the electrons from the radiation, removing that background. Unless otherwise stated, all phase spaces reported here were measured using the Faraday cup in the C2 section.

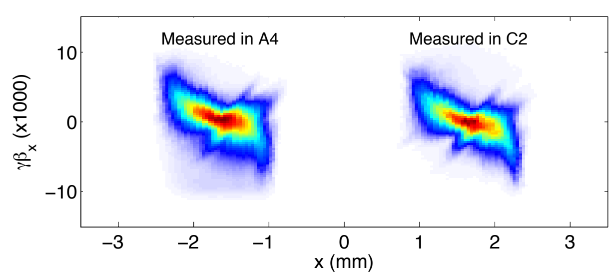

FIG. 6. Comparison of the measured phase space using the A4 and C2 Faraday cups. The 100% emittance in both images is 0.802 μm and 0.785 μm, respectively.

B. Final Measurements

For each bunch charge we loaded the corresponding optimal settings into the injector and tuned the machine to produce the lowest emittances possible while still meeting the peak current targets. All critical machine parameters matched those chosen by the optimizer to within 5%, with the notable exception of the pinhole used for the 20 pC measurements. At these optimal machine settings, we measured the initial transverse laser distribution at the cathode, as well as the longitudinal electron current distribution, and both the horizontal and vertical projected phases spaces at the EMS.

Fig. 7 displays the measured horizontal and vertical projected phases spaces corresponding to the best measured emittances. Note the use of the normalized mechanical momenta $\gamma\beta_{x_i} = p_{x_i}/mc$. One striking feature seen in Fig. 7 is the overall symmetry between the horizontal and vertical phase spaces. Fig. 8 shows the comparison of the measured (red) and simulated longitudinal current profiles (blue). In addition to the excellent agreement seen between measurement and simulation, we note that all peak current targets were met.

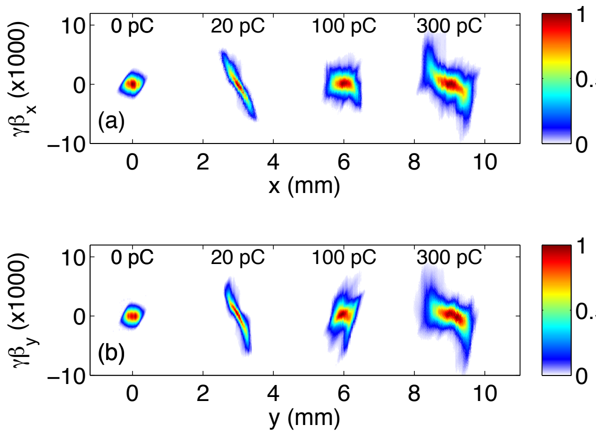

FIG. 7. Measured horizontal (a) and vertical (b) projected phase spaces.

Table III displays the thermal and core emittance at the cathode and the resulting measured 95% (Table-III(a)) and core emittances (Table-III(b)) at the EMS. We estimate a ±6% relative error for the thermal emittances due to possible error in the measurement of the laser path length, as well as the error in the measured MTE. For the EMS system we estimate a ±10% relative error in the 95% emittances measured with the EMS (up to the specified resolution of ≤ 0.05 μm) due scanner calibration. For the charges and injector optics in these measurements, envelope analysis [3] shows that the EMS over estimates the measured emittance due to space charge induced expansion of the beamlet passing between the two EMS slits. A conservative estimate shows this effect to be less than a few percent of the measured emittance values. The random error between subsequent measurements using the EMS was typically ≤1%. We note that data in Table III quantitatively reflects the qualitative symmetry seen in the phase space measurements (Fig. 7), and as well as satisfies all of the LCLS-II injector emittance targets. The table also shows the ratio of the thermal emittance and the final 95% emittance, and the ratio of the initial and final core emittances. In all measurements, the thermal emittances were preserved to within 58%-80%. Similarly, the core emittances were preserved within 67-87%. We point out that the roughly 80-90% preservation of the core emittance for all charges except 20 pC. In this case, the finite resolution of the EMS ($\leq$ 0.05 μm) likely becomes a contributing factor when measuring such small emittances. We conclude that the actual core emittance for this bunch charge is smaller than the quoted value, as suggested by simulation. Nevertheless, these results demonstrate the main focus of this work: contrary to previous thought, DC gun based photoinjectors are capable of delivering cathode emittance dominated beams at high bunch charges suitable for use in next generation FELs like the LCLS-II.

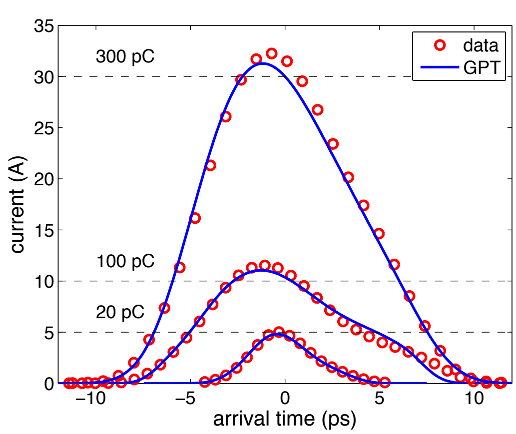

FIG. 8. Comparison of the simulated (blue) and measured (red) current profiles as a function of bunch charge. Peak current targets are shown in black.

TABLE III. (a) Measured horizontal (vertical) thermal 95% emittances at the EMS location. (b) Initial and final measured horizontal (vertical) core emittances.

(a) Horizontal (vertical) projected emittance data.

Charge	Thermal ϵ_n (μm)	95% ϵ_n (μm)	Ratio (%)
20 pC	0.12 (0.11)	0.18 (0.19)	67 (58)
100 pC	0.24 (0.23)	0.30 (0.32)	80 (72)
300 pC	0.42 (0.41)	0.62 (0.60)	67 (68)

(b) Horizontal (vertical) projected core emittance data.

Charge	Cathode $\epsilon_{n,\text{core}}$ (μm)	EMS $\epsilon_{n,\text{core}}$ (μm)	Ratio (%)
20 pC	0.06 (0.06)	0.09 (0.08)	67 (75)
100 pC	0.14 (0.13)	0.16 (0.16)	85 (79)
300 pC	0.26 (0.24)	0.30 (0.28)	87 (87)

Previous work [9] shows that the specific shape of the laser distribution effects the symmetry and linearity of the space charge forces, and thus the degree of emittance preservation, even though the cathode emittance (Eqn. 1) remains unchanged for laser distributions with the same rms spot size. In order to determine the effect of quality of the laser shape on the measured emittances in this work, we ran a second round of optimiza-

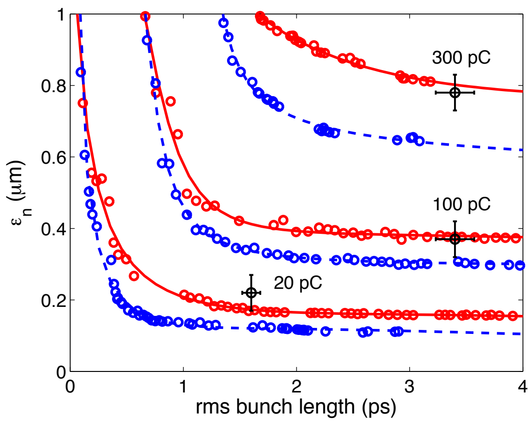

FIG. 9. Optimized emittance vs. rms bunch length at the EMS using (blue) a perfect variable truncated Gaussian and variable temporal distribution, (red) the measured laser distributions. Measured data are shown in black.

tions using the measured transverse laser distributions in Fig. 2(a) and the crystal angles used to create the flat-top in Fig. 2(b). All other relevant injector parameters varied as before. Fig. 9 shows the *average 100% emittance*, $\epsilon_n = \frac{1}{2}(\epsilon_{n,x} + \epsilon_{n,y})$, vs. rms bunch length at the EMS for each bunch charge. Shown in blue are the initial optimizations with varied laser distribution parameters, and ideal transverse shape. The red curves show the results of the second round of optimizations using the measured laser distributions (Fig. 2). The emittances corresponding to the data in Figs. 7-8 and Table-III are shown in black. We note that the growth in the optimized emittances at the EMS arising from the imperfections in the measured transverse laser distributions (distance between blue and red curves at the measured bunch lengths shown in black) increases with bunch charge, as one might expect. For the 100 and 300 pC measurements, this produces roughly a 23%, and 27% relative emittance growth, due primarily to imperfections in transverse laser shape (as opposed to using a non-optimal pinhole size). In the 20 pC case, the 42% relative emittance growth seen is likely due to the use of a pinhole size 40% larger than the optimal value.

In concluding this section, we point out that the optimal injector settings found using MOGA optimizations of 3D space charge simulations of the Cornell ERL injector produce machine states that preserve both the measured 95% and core emittance, computed from direct phase space measurements, to within 57-87% for 20, 100, 300 pC bunches. Furthermore, the resulting measured emittances and longitudinal current profile show excellent agreement with corresponding GPT simulations, and meet the stated 95% emittance and peak current specifications of the LCLS-II injector design. Additionally, we have shown that the transverse laser shape plays an important role in determining the optimal emittances, adding further relevance to the recent demonstration of accurate, arbitrary transverse laser shaping at Cornell [10, 11]. In conclusion, this work shows that DC gun based photoinjectors can produce cathode emittance dominated beams with single bunch beam quality rivaling that produced by RF gun based injectors for charges up to 300 pC, and represents a significant expansion of the beam dynamics regime for which DC gun-based injectors are applicable.

II. LCLS-II INJECTOR LAYOUT OPTIMIZATIONS

Multi-objective genetic algorithm optimizations using ASTRA were run to compare various layout and cryomodule designs for the LCLS-II injector. All simulations were run with a 300 pC bunch charge, 10k macroparticles, and cylindrically symmetric field maps. Four layouts were chosen for comparison, each with a short and long warm section. These are described in Fig. 10. A short warm section corresponds to using the Cornell solenoids and buncher, while a long warm section corresponds to using the LBL solenoids and buncher. All emittance plots in this section (Figures 11-13) show the 100% emittance. Figure-7 shows the comparison of

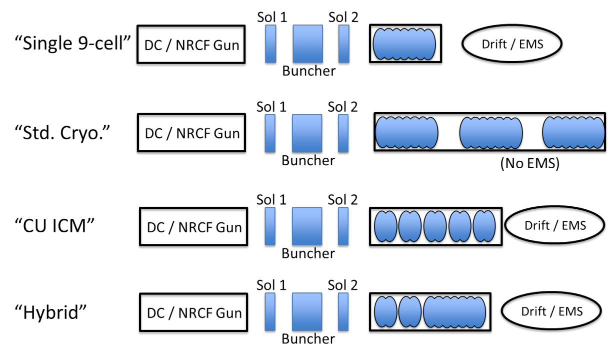

FIG. 10. Schematic of the various layouts to optimize.

various layouts with a DC gun and Cornell warm section to the baseline design with a 750 kV RF gun (blue). It is important to note that the current Cornell injector (orange) meets the LCLS-II specs, as now verified with measurement. In addition, a 500 kV DC gun with a single 9-cell cavity (red) would give comparable performance to the baseline design or current Cornell injector. Figure-8 shows the comparison of the baseline design, a single-9 cell capture cavity, and the Cornell Hybrid design all with the LBL warm section and a 750 kV gun. The results show that using a single 9-cell capture cavity (red) can improve the emittance by roughly 20

In summary:

1. The baseline design meets the specifications with a 750 kV RF gun.

2. Having a single isolated booster cavity improves emittance by 20% and allows room for low energy

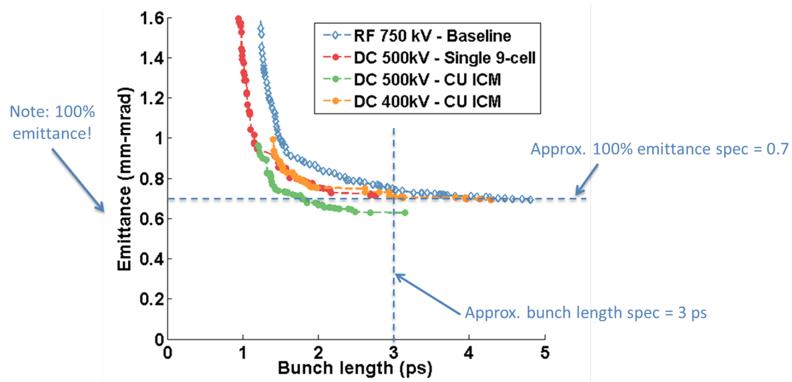

FIG. 11.

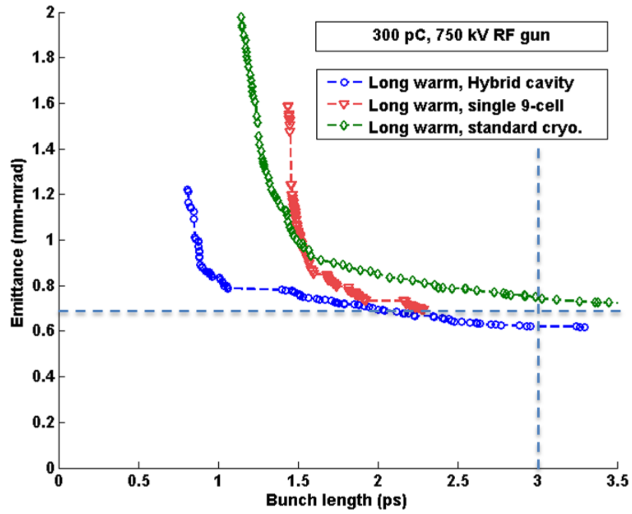

FIG. 12. Comparison of the 100% emittance vs. bunch length for different cryomodules using the LBL warm section and a 750 kV gun

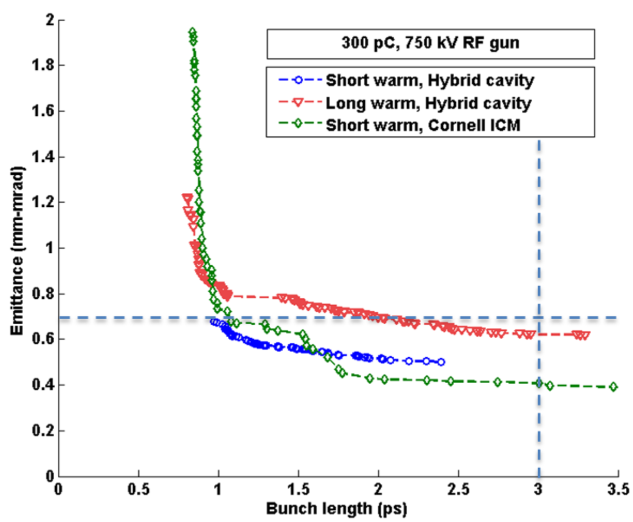

FIG. 13. Comparison of 100% emittance vs. bunch length for various cryomodules using either a short (Cornell) or long (LBL) warm section and the 750 kV gun.

emittance and beam diagnostics. From the point of view of commissioning, these are highly recommended.

3. Shortening the warm section of the injector can improve emittance 20-30%.

III. SEGMENTED GUN MEASUREMENTS

The Cornell segmented gun had been processed up to a maximum (unstable) conditioning value of 550 kV in vacuum. The conditioning process lasted for more than 140 hours, as shown Fig. 14. For a full description of this

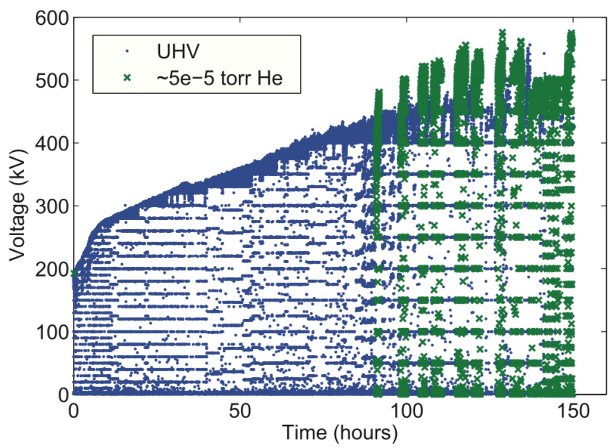

FIG. 14. The voltage applied to the gun during conditioning, corrected for the voltage drop across the processing resistor. Data points are colored for UHV (blue dot) and helium gas (green x) conditioning.

conditioning process, see [12].

Following processing, a low current beam has been demonstrated at 400 kV. Both the transverse emittance measurement system (EMS) and deflecting cavity on the segmented gun diagnostic beam line have been commissioned and calibrated at low charge. Mechanical solenoid alignment was performed, which allowed the measurement of thermal emittance via solenoid scan from the NaKSb photocathode used in the injector measurements [13]. A proof of principle high precision laser shaping setup using a spatial light modulator was demonstrated [11]. Finally, a mechanical issue with the high voltage stalk support plate has been determined to be the cause of photocathode loading difficulties. The gun was vented and this stalk support plate has been replaced, and photocathode loading and electrode stability are much improved.

After this initial commissioning, high bunch charge emittance measurements were performed. Two data sets were produced using either 4 or 5 longitudinal laser shaping crystals (8 ps or 25 ps rms laser pulse length respectively). For each dataset, the vertical phase space was measured using the EMS, located meters from the cathode. Fig. 15 shows the results of these measurements as

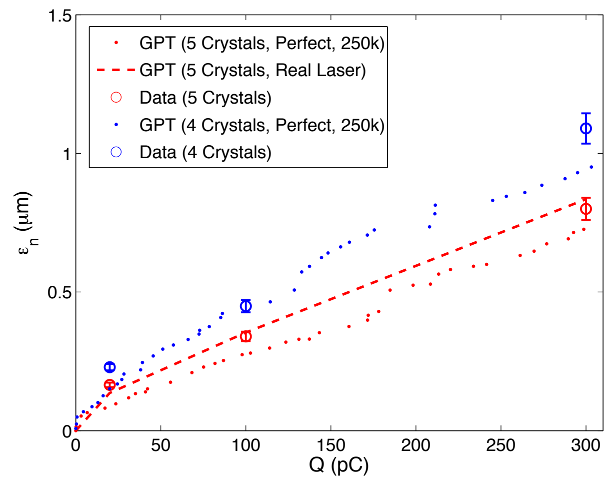

FIG. 15. Optimized emittance vs. bunch charge at the EMS using the two crystal sets. The dotted lines show the optimized GPT simulations using a perfect laser shape. The dashed red line shows the GPT simulations using the measured laser shape (for the 5 crystal set).

well as the optimized emittance, simulated with GPT, as a function of bunch charge. Good agreement with simulation was found in both cases. Table IV shows the 95% emittance values recorded as a function of bunch charge. Note that in these measurements the emittances at 20

TABLE IV. Segmented Gun Vertical Emittance Measurements for the 5 (4) Crystal Set

Bunch Charge	20 pC	100 pC	300 pC
95% $\epsilon_{n,y}$ (μm)	0.13 (0.18)	0.27 (0.35)	0.65 (0.81)
100% $\epsilon_{n,y}$ (μm)	0.17 (0.23)	0.34 (0.45)	0.8 (1.1)

and 100 pC already meet the LCLS-II specifications for both crystal sets (laser pulse lengths), without the aid of the bunching and SRF cavities, as well as the second solenoid for emittance compensation. These results demonstrate that the segmented gun operating at 400 kV can meet the emittance specifications for LCLS-II.

ACKNOWLEDGMENTS

This work was supported, in part, by the LCLS-II Project and the US Department of Energy, Contract DE-AC02-76SF00515.

[1] B. Dunham, J. Barley, A. Bartnik, I. Bazarov, L. Cultrera, J. Dobbins, G. Hoffstaetter, B. Johnson, R. Kaplan, S. Karkare, V. Kostroun, Y. Li, M. Liepe, X. Liu, F. Loehl, J. Maxson, P. Quigley, J. Reilly, D. Rice, D. Sabol, E. Smith, K. Smolenski, M. Tigner, V. Vesherevich, D. Widger, and Z. Zhao, Applied Physics Letters **102**, 034105 (2013).

[2] C. Gulliford, A. Bartnik, I. Bazarov, L. Cultrera, J. Dobbins, B. Dunham, F. Gonzalez, S. Karkare, H. Lee, H. Li, Y. Li, X. Liu, J. Maxson, C. Nguyen, K. Smolenski, and Z. Zhao, Phys. Rev. ST Accel. Beams **16**, 073401 (2013).

[3] I. V. Bazarov, B. M. Dunham, C. Gulliford, Y. Li, X. Liu, C. K. Sinclair, K. Soong, and F. Hannon, Phys. Rev. ST Accel. Beams **11**, 100703 (2008).

[4] Z. Zhao, B. M. Dunham, I. Bazarov, and F. W. Wise, Opt. Express **20**, 4850 (2012).

[5] L. Cultrera, S. Karkare, B. Lillard, A. Bartnik, I. Bazarov, B. Dunham, W. Schaff, and K. Smolenski, Applied Physics Letters **103**, 103504 (2013).

[6] I. Bazarov, L. Cultrera, A. Bartnik, B. Dunham, S. Karkare, Y. Li, X. Liu, J. Maxson, and W. Roussel, Applied Physics Letters **98**, 224101 (2011).

[7] "Pulsar website for gpt," `http://www.pulsar.nl/gpt/` (2011).

[8] D. Dowell, "Private communication,".

[9] F. Zhou, A. Brachmann, P. Emma, S. Gilevich, and Z. Huang, Phys. Rev. ST Accel. Beams **15**, 090701 (2012).

[10] J. M. Maxson, A. C. Bartnik, and I. V. Bazarov, Appl. Phys. Lett. **105** (2014).

[11] J. Maxson, H. Lee, A. C. Bartnik, J. Kiefer, and I. Bazarov, Phys. Rev. ST Accel. Beams **18**, 023401 (2015).

[12] J. Maxson, I. Bazarov, B. Dunham, J. Dobbins, X. Liu, and K. Smolenski, Review of Scientific Instruments **85**, 093306 (2014).

[13] J. Maxson, L. Cultrera, C. Gulliford, and I. Bazarov, Applied Physics Letters **106**, 234102 (2015).